Hydride Transfer in Liver Alcohol Dehydrogenase: Quantum Dynamics, Kinetic Isotope Effects, and Role of Enzyme Motion

Salomon R. Billeter, Simon P. Webb, Pratul K. Agarwal, Tzvetelin Iordanov, and Sharon Hammes-Schiffer*

Contribution from the Department of Chemistry, 152 Davey Laboratory, Pennsylvania State University, University Park, Pennsylvania 16802

Received June 5, 2001

Abstract: The quantum dynamics of the hydride transfer reaction catalyzed by liver alcohol dehydrogenase (LADH) are studied with real-time dynamical simulations including the motion of the entire solvated enzyme. The electronic quantum effects are incorporated with an empirical valence bond potential, and the nuclear quantum effects of the transferring hydrogen are incorporated with a mixed quantum/classical molecular dynamics method in which the transferring hydrogen nucleus is represented by a three-dimensional vibrational wave function. The equilibrium transition state theory rate constants are determined from the adiabatic quantum free energy profiles, which include the free energy of the zero point motion for the transferring nucleus. The nonequilibrium dynamical effects are determined by calculating the transmission coefficients with a reactive flux scheme based on real-time molecular dynamics with quantum transitions (MDQT) surface hopping trajectories. The values of nearly unity for these transmission coefficients imply that nonequilibrium dynamical effects such as barrier recrossings are not dominant for this reaction. The calculated deuterium and tritium kinetic isotope effects for the overall rate agree with experimental results. These simulations elucidate the fundamental nature of the nuclear quantum effects and provide evidence of hydrogen tunneling in the direction along the donor–acceptor axis. An analysis of the geometrical parameters during the equilibrium and nonequilibrium simulations provides insight into the relation between specific enzyme motions and enzyme activity. The donor–acceptor distance, the catalytic zinc–substrate oxygen distance, and the coenzyme (NAD$^+$/NADH) ring angles are found to strongly impact the activation free energy barrier, while the donor–acceptor distance and one of the coenzyme ring angles are found to be correlated to the degree of barrier recrossing. The distance between VAL-203 and the reactive center is found to significantly impact the activation free energy but not the degree of barrier recrossing. This result indicates that the experimentally observed effect of mutating VAL-203 on the enzyme activity is due to the alteration of the equilibrium free energy difference between the transition state and the reactant rather than nonequilibrium dynamical factors. The promoting motion of VAL-203 is characterized in terms of steric interactions involving THR-178 and the coenzyme.

I. Introduction

Liver alcohol dehydrogenase (LADH) catalyzes the reversible oxidation of alcohols to the corresponding aldehydes or ketones. The key step in this enzyme reaction is the transfer of a hydride between the substrate and the coenzyme nicotinamide adenine dinucleotide (NAD$^+$). Kinetic isotope effect experiments on the LADH-catalyzed oxidation of benzyl alcohol indicate that nuclear quantum effects are significant for this hydride transfer reaction.[1,2] In the interpretation of these experiments, hydrogen tunneling is implicated by deviations from semiclassical predictions.[2] Furthermore, the investigation of site-directed mutants has provided evidence of a link between hydrogen tunneling and the enzyme structure.[3] Specifically, the rate of hydride transfer decreases when VAL-203 is replaced by the smaller residue alanine.

Several theoretical studies have been directed toward the investigation of nuclear quantum effects in LADH. Rucker and

Klinman developed a simple model to study the oxidation of benzyl alcohol by yeast alcohol dehydrogenase.[4] Although this model did not include the enzyme, it provided insight into the basis for the experimentally observed kinetic isotope effects. More recently, Gao, Truhlar, and co-workers used canonical variational transition state theory with semiclassical tunneling corrections to study the oxidation of benzyl alcohol by LADH.[5] Their calculations were based on a mixed quantum mechanical/molecular mechanical (QM/MM) potential. The semiclassical quantum dynamics corrections were calculated for a 21-atom portion of the system embedded in the potential of a frozen secondary zone and were averaged over 20 secondary-zone configurations. Their calculated primary and secondary kinetic isotope effects are consistent with the experimentally measured values. In ref 6, the nuclear quantum effects in the oxidation of benzyl alcohol by LADH were investigated by calculating the hydrogen vibrational wave functions for structures along minimum energy paths and straight-line reaction paths obtained from electronic structure calculations for a 148-atom model of

---

* Corresponding author. E-mail: shs@chem.psu.edu.
(1) Bahnson, B. J.; Park, D.-H.; Kim, K.; Plapp, B. V.; Klinman, J. P. *Biochemistry* **1993**, *32*, 5503.
(2) Bahnson, B. J.; Klinman, J. P. *Methods Enzymol.* **1995**, *249*, 374.
(3) Bahnson, B. J.; Colby, T. D.; Chin, J. K.; Goldstein, B. M.; Klinman, J. P. *Proc. Natl. Acad. Sci. U.S.A.* **1997**, *94*, 12797. Note that the interpretation of these experiments may not be definitive due to the complexity of the reaction.

(4) Rucker, J.; Klinman, J. P. *J. Am. Chem. Soc.* **1999**, *121*, 1997.
(5) Alhambra, C.; Corchado, J. C.; Sanchez, M. L.; Gao, J.; Truhlar, D. G. *J. Am. Chem. Soc.* **2000**, *122*, 8197.
(6) Webb, S. P.; Agarwal, P. K.; Hammes-Schiffer, S. *J. Phys. Chem. B* **2000**, *104*, 8884.

the active site. These studies provided information about the fundamental nature of the nuclear quantum effects, the dominant contributions to the reaction coordinate, and the factors that impact hydrogen tunneling in this reaction. Finally, Bruice and co-workers have used classical molecular dynamics simulations to probe the impact of mutations on the hydride transfer reaction in LADH. In particular, they calculated the close contact distances between the alcohol substrate and NAD$^+$ for native LADH and for LADH with mutations of the VAL-203 site.[7]
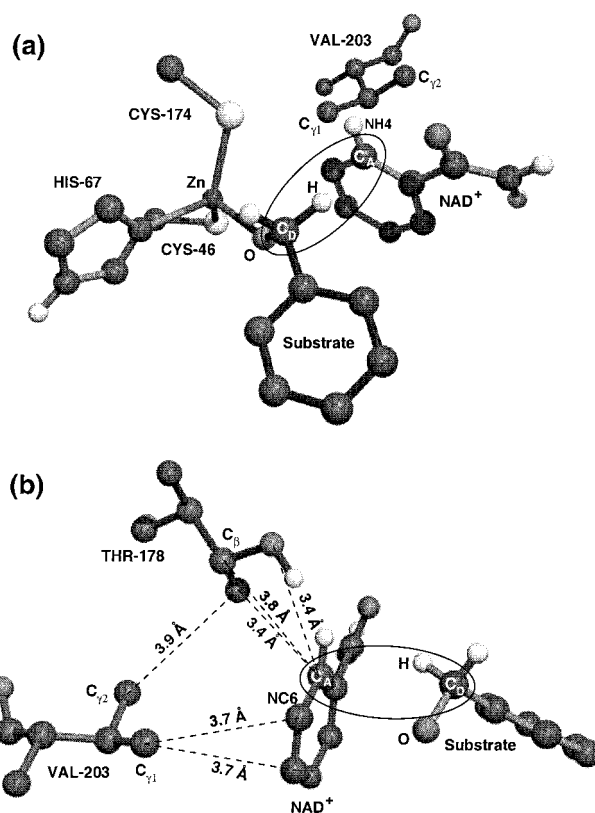
In ref 8, a new hybrid approach was implemented to study the quantum dynamics of the LADH-catalyzed oxidation of benzyl alcohol. This paper utilizes this hybrid approach to calculate the dynamical kinetic isotope effects and to investigate the role of specific enzyme motions for this reaction. This hybrid approach incorporates both electronic and nuclear quantum effects into real-time dynamical simulations that include the motion of the entire solvated enzyme (75140 atoms). The electronic quantum effects are included with an empirical valence bond (EVB) potential to allow chemical bonds to break and form. The nuclear quantum effects of the transferring hydrogen are included with a mixed quantum/classical molecular dynamics method in which the transferring hydrogen nucleus is represented by a three-dimensional vibrational wave function.

In this hybrid approach, the rates are obtained by calculating both a transition state theory rate constant, which is determined from the activation free energy, and a transmission coefficient, which accounts for dynamical recrossings of the free energy barrier. The activation free energy is calculated from equilibrium molecular dynamics simulations that provide the free energy profile as a function of a collective reaction coordinate. The transmission coefficient is calculated with a reactive flux scheme based on an ensemble of real-time dynamical trajectories propagated with the molecular dynamics with quantum transitions (MDQT) surface hopping method. This approach accounts for dynamical recrossings of the free energy barrier, while including vibrationally nonadiabatic effects and the dynamics of the complete solvated enzyme. Moreover, these calculations provide information about the fundamental nature of the nuclear quantum effects (i.e., the significance of zero point motion and hydrogen tunneling).

In addition to predicting rates and kinetic isotope effects, this hybrid approach elucidates the impact of specific motions of the enzyme on the activation free energy barrier and on the degree of dynamical barrier recrossing. The comparison of equilibrium and nonequilibrium dynamical effects of the enzyme provides information about the relative time scales of the specific motions. The analysis in this paper centers on the donor−acceptor (C$_D$–C$_A$) vibration, the NAD$^+$/NADH out-of-plane ring angles, the catalytic zinc−substrate oxygen (Zn−O) distance, the donor carbon−oxygen (C$_D$–O) distance within the substrate, and the VAL-203 motion. This analysis provides insight into the fundamental mechanism of LADH, as well as the basis for the experimentally observed kinetic isotope effects.

II. Methods

The system used in our LADH calculations contains the protein dimer, two NAD$^+$ cofactors, two benzyl alkoxide substrates, four zinc ions, and 22 682 water molecules in a rectangular periodic box with edge lengths of 73.13, 85.53, and 125.30 Å. The active site of LADH is depicted in Figure 1. In this paper, we assume that the reaction is electronically adiabatic and use a Born−Oppenheimer separation of the electrons and nuclei. The quantum effects of the electrons are

(7) Luo, J.; Kahn, K.; Bruice, T. C. *Bioorg. Chem.* **1999**, *27*, 289.
(8) Billeter, S. R.; Webb, S. P.; Iordanov, T.; Agarwal, P. K.; Hammes-Schiffer, S. *J. Chem. Phys.* **2001**, *114*, 6925.

Figure 1. A portion of the crystal structure[38] of the active site of horse liver alcohol dehydrogenase with NAD$^+$ and benzyl alkoxide, where the positions of the heavy atoms of the substrate correspond to those of pentafluorobenzyl alcohol. The circle identifies the reaction core, consisting of the donor carbon atom C$_D$, the transferring hydride H, and the acceptor carbon atom C$_A$. C$_{\gamma 1}$ is defined to be the C$_\gamma$ of VAL-203 closest to C$_A$. Two different perspectives are shown.

included with an empirical valence bond (EVB) potential,[9] and the quantum effects of the transferring hydrogen nucleus are included by treating this nucleus as a multidimensional vibrational wave function.[10] In this section, we briefly outline the approach for the inclusion of both electronic and nuclear quantum effects, as well as the methodology for the generation of the free energy profiles and the calculation of dynamical effects. The details of all methodology, including the parameters and relevant equations, are given in ref 8.

A. Electronic and Nuclear Quantum Effects. We use an empirical valence bond (EVB) potential to include the electronic quantum effects required to describe the breaking and forming of chemical bonds. In the EVB approach,[9] the ground state electronic wave function is expanded in a basis of VB states, and the corresponding potential energy surface $V_{el0}(\mathbf{r}, \mathbf{R})$ is the lowest eigenvalue of the Hamiltonian matrix in this basis set. (Here $\mathbf{r}$ denotes the coordinates of the transferring hydrogen nucleus and $\mathbf{R}$ denotes the coordinates of all other nuclei in the system.) In this paper, the basis set consists of the two VB states shown in Figure 2. In VB state 1 the hydride is bonded to its donor carbon, while in VB state 2 the hydride is bonded to its acceptor carbon. The Hamiltonian matrix is expressed in this basis set as

$$\tilde{\mathbf{H}}(\mathbf{r}, \mathbf{R}) = \begin{pmatrix} V_{11}(\mathbf{r}, \mathbf{R}) & V_{12}(\mathbf{r}, \mathbf{R}) \\ V_{12}(\mathbf{r}, \mathbf{R}) & V_{22}(\mathbf{r}, \mathbf{R}) \end{pmatrix} \tag{1}$$

The matrix elements $V_{ii'}(\mathbf{r}, \mathbf{R})$ are represented as parametrized analytical functional forms. The diagonal elements are described by the GROMOS force field 43A1[11] with modifications described in ref 8. The electrostatic and Lennard-Jones interactions are treated consistently with the GROMOS force field. The cutoff radius for nonbonded interactions is

(9) Warshel, A. *Computer Modeling of Chemical Reactions in Enzymes and Solutions;* John Wiley: New York, 1991.
(10) Webb, S. P.; Hammes-Schiffer, S. *J. Chem. Phys.* **2000**, *113*, 5214.
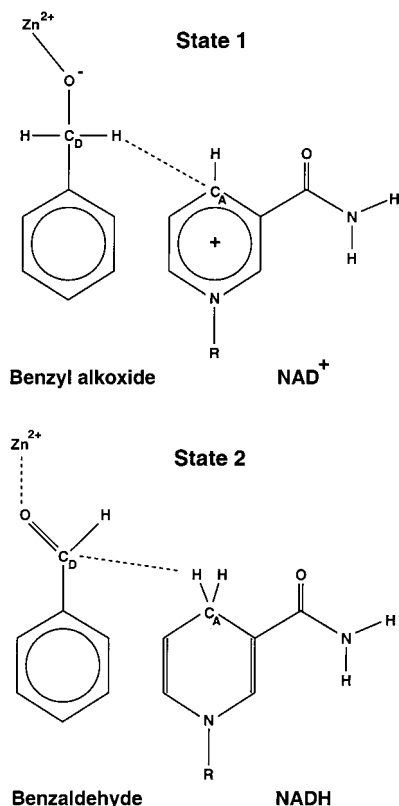
Figure 2. Valence bond structures for the hydride transfer reaction between zinc-bound benzyl alkoxide and NAD$^+$.

14 Å, and the nonbonded interactions between 8 and 14 Å are calculated only every 5 molecular dynamics steps, along with updating the charge-group based nonbonded interactions pair list. Outside the sphere of radius 14 Å, the electrostatics are represented by a reaction field with a relative dielectric constant of 54 and a zero inverse Debye screening length. The off-diagonal element is assumed to be a constant V_{12}, and a constant energy adjustment Δ_{12} is included in $V_{22}(\mathbf{r}, \mathbf{R})$. Both V_{12} and Δ_{12} have been chosen to ensure that the quantum free energy profile for the reaction reproduces the experimental free energies of reaction and activation. The parameters for the EVB potential used for the calculations in this paper are provided in ref 8.

We incorporate the nuclear quantum effects of the transferring hydrogen into our simulations by treating this nucleus as a multidimensional vibrational wave function. For this purpose, we use a mixed quantum/classical description of the nuclei, in which the transferring hydrogen nucleus with coordinate $\mathbf{r}$ is treated quantum mechanically, while the remaining nuclei with coordinates $\mathbf{R}$ are treated classically. The adiabatic vibrational wave functions for the transferring hydrogen can be calculated for fixed classical coordinates $\mathbf{R}$ by solving the time-independent Schrödinger equation

$$[T_{\mathrm{H}} + V_{\mathrm{el0}}(\mathbf{r}, \mathbf{R})]\Phi_j(\mathbf{r}; \mathbf{R}) = \epsilon_j(\mathbf{R})\Phi_j(\mathbf{r}; \mathbf{R}) \qquad (2)$$

where T_{H} is the kinetic energy of the transferring hydrogen and $V_{\mathrm{el0}}(\mathbf{r}, \mathbf{R})$ is the potential energy of the electronic ground state. In this paper we include the nonadiabatic effects from the excited vibrational states to allow an accurate calculation of the hydrogen quantum effects. Thus, eq 2 is solved for a range of states j.

As will be described below, eq 2 must be solved for each configuration of the classical nuclei during the generation of the free energy profiles and during the dynamical calculation of the transmission coefficient. To facilitate this calculation, we use the state-averaged

Fourier grid Hamiltonian multiconfigurational self-consistent-field (FGH-MCSCF) method for calculating multidimensional hydrogen vibrational wave functions.[10] Moreover, to further decrease the computational expense, we utilize a partial multidimensional grid generation method to decrease the number of potential energy calculations by avoiding these calculations for grid points with high potential energy.[12] This approach accurately describes ground and excited state hydrogen vibrational wave functions in a computationally practical manner. For the calculations presented in this paper, the transferring hydride is represented on a three-dimensional cubic grid centered between the donor and acceptor carbon atoms. The length of each side of the cubic grid is 4.76 Å, with 64 grid points/spatial dimension. For the FGH-MCSCF calculations, the active space is spanned by 5 one-dimensional states per dimension, and the wave function is calculated by state-averaging over the lowest 4 multiconfigurational states. A cutoff of 94.1 kcal/mol for the potential energy is used for the partial multidimensional grid generation.

B. Free Energy Profiles. To calculate the transition state theory rate constant, the free energy profile must be calculated. The transition state theory rate constant is[13]

$$k_{\mathrm{TST}} = \frac{k_{\mathrm{B}}T}{h}\mathrm{e}^{-\Delta G^{\dagger}/k_{\mathrm{B}}T} \qquad (3)$$

where $\Delta G^{\dagger}$ is the free energy barrier for the reaction and k_{B} is Boltzmann's constant. Since the hydride transfer reaction involves a free energy barrier that is significantly larger than the thermal energy, a mapping potential is used to drive the system over the barrier. Similar to previous work of Warshel and co-workers,[9] we define a mapping potential $V_{\mathrm{map}}(\mathbf{r}, \mathbf{R}; \lambda)$ as

$$V_{\mathrm{map}}(\mathbf{r}, \mathbf{R}; \lambda) = (1 - \lambda)V_{11}(\mathbf{r}, \mathbf{R}) + \lambda V_{22}(\mathbf{r}, \mathbf{R}) \qquad (4)$$

where V_{11} and V_{22} are the diagonal elements of the EVB Hamiltonian in eq 1. As the parameter λ is varied from zero to unity, the reaction progresses from the reactant VB state 1 to the product VB state 2. In this paper, we calculate both the classical free energy profile, corresponding to the classical treatment of the transferring hydrogen nucleus, and the quantum free energy profile, corresponding to the quantum mechanical treatment of the transferring hydrogen nucleus. A comparison of the classical and quantum free energy profiles provides an indication of the significance of nuclear quantum effects.

We calculate the free energy profiles as functions of a collective reaction coordinate analogous to the solvent coordinate used in standard Marcus theory for electron transfer reactions.[14−17] When the transferring hydrogen is treated classically, this collective reaction coordinate is defined as

$$\Lambda^{(\mathrm{c})}(\mathbf{r}, \mathbf{R}) = V_{22}(\mathbf{r}, \mathbf{R}) - V_{11}(\mathbf{r}, \mathbf{R}) \qquad (5)$$

In this case, the reaction coordinate depends on both $\mathbf{r}$ and $\mathbf{R}$. When the transferring hydrogen is treated quantum mechanically, the reaction coordinate should not be a function of the quantum coordinate $\mathbf{r}$ since the classical molecular dynamics samples the configurational space of only the classical coordinates $\mathbf{R}$. Moreover, the reaction coordinate $\Lambda^{(\mathrm{c})}(\mathbf{r}, \mathbf{R})$ defined in eq 5 does not distinguish between symmetric and asymmetric hydrogen potential energy surfaces (or hydrogen vibrational wave functions), as required in the framework of standard Marcus theory.[14] Thus, the physically meaningful reaction coordinate when the transferring hydrogen nucleus is treated quantum mechanically is defined as

$$\Lambda^{(\mathrm{q})}(\mathbf{R}) = \langle\Phi_0(\mathbf{r}; \mathbf{R})|V_{22}(\mathbf{r}, \mathbf{R}) - V_{11}(\mathbf{r}, \mathbf{R})|\Phi_0(\mathbf{r}; \mathbf{R})\rangle_{\mathrm{r}} \qquad (6)$$

(11) van Gunsteren, W. F.; Billeter, S. R.; Eising, A. A.; Hünenberger, P. H.; Krüger, P.; Mark, A. E.; Scott, W. R. P.; Tironi, I. G. *Biomolecular Simulation: The GROMOS96 Manual and User Guide;* Biomos b.v., Zürich and Groningen, VdF Hochschulverlag, ETH Zürich: Zürich, 1996.

(12) Iordanov, T.; Billeter, S. R.; Webb, S. P.; Hammes-Schiffer, S. *Chem. Phys. Lett.* **2001**, *338*, 389.

(13) Wigner, E. *Phys. Rev.* **1932**, *40*, 749.

(14) Marcus, R. A. *Annu. Rev. Phys. Chem.* **1964**, *15*, 155.

(15) Zusman, L. D. *Chem. Phys.* **1980**, *49*, 295.

(16) Warshel, A. *J. Phys. Chem.* **1982**, *86*, 2218.

(17) King, G.; Warshel, A. *J. Chem. Phys.* **1990**, *93*, 8682.

where $\langle \cdots \rangle_r$ indicates integration over the quantum coordinate $\mathbf{r}$ and $\Phi_0(\mathbf{r}; \mathbf{R})$ is the ground state vibrational wave function. Note that, in practice, the classical and quantum reaction coordinates are divided into discrete intervals (i.e., bins) represented by values Λ_n.

The calculation of the classical free energy profile for the electronic ground state potential $V_{el0}(\mathbf{r}, \mathbf{R})$ consists of three steps.[8] In the first step, the free energy $F_{map}(\Lambda_n; \lambda_m)$ for the mapping potential along the reaction coordinate $\Lambda^{(c)}(\mathbf{r}, \mathbf{R})$ defined in eq 5 is calculated for each λ_m using a standard binning procedure[19] during molecular dynamics simulations governed by $V_{map}(\mathbf{r}, \mathbf{R}; \lambda_m)$. In the second step, the relative free energies for the mapping potential corresponding to the same value of Λ_n but different values of λ_m are determined from thermodynamic integration.[20] Note that this procedure avoids the arbitrary translation of the individual segments of the free energy profile corresponding to different values of λ_m. Moreover, the degree of overlap of the neighboring segments provides an indication of the convergence of the calculations. In the third step, the classical free energy $F_{el0}(\Lambda_n; \lambda_m)$ for the electronic ground state potential $V_{el0}(\mathbf{r}, \mathbf{R})$ is calculated from the molecular dynamics simulations governed by the mapping potential using a perturbation formula.

For the generation of the quantum free energy profiles, only vibrationally adiabatic nuclear quantum effects are included. We calculate the free energy associated with the energy of the ground state hydrogen vibrational wave function, defined as $\epsilon_0(\mathbf{R})$ in eq 2. The quantum free energy $F_{el0,nuc0}(\Lambda_n; \lambda_m)$ associated with this potential energy is calculated from the perturbation formula

$$e^{-\beta F_{el0,nuc0}(\Lambda_n; \lambda_m)} = e^{-\beta F_{map}(\Lambda_n; \lambda_m)} \langle e^{-\beta[\epsilon_0(\mathbf{R}) - V_{intmap}(\mathbf{R}; \lambda_m)]} \rangle_{\lambda_m, \Lambda_n, q} \quad (7)$$

The angular brackets are defined by

$$\langle f(\mathbf{r}, \mathbf{R}) \rangle_{\lambda_m, \Lambda_n, q} = \frac{\int d\mathbf{r} \int d\mathbf{R} \, \delta(\Lambda^{(q)}(\mathbf{r}, \mathbf{R}) - \Lambda_n) f(\mathbf{r}, \mathbf{R}) e^{-\beta V_{map}(\mathbf{r}, \mathbf{R}; \lambda_m)}}{\int d\mathbf{r} \int d\mathbf{R} \, \delta(\Lambda^{(q)}(\mathbf{r}, \mathbf{R}) - \Lambda_n) e^{-\beta V_{map}(\mathbf{r}, \mathbf{R}; \lambda_m)}} \quad (8)$$

where $\delta(\Lambda^{(q)}(\mathbf{r}, \mathbf{R}) - \Lambda_n)$ is a unitless quantity equal to unity if $\Lambda^{(q)}(\mathbf{r}, \mathbf{R})$ is within the bin represented by Λ_n and zero otherwise and $V_{intmap}(\mathbf{R}; \lambda)$ is defined by

$$e^{-\beta V_{intmap}(\mathbf{R}; \lambda_m)} = C_{\mathbf{r}} \int d\mathbf{r} \, e^{-\beta V_{map}(\mathbf{r}, \mathbf{R}; \lambda_m)} \quad (9)$$

with $C_{\mathbf{r}}$ a constant of dimension inverse volume in the coordinate space $\mathbf{r}$. The derivation of this perturbation formula is given in ref 8. (Note that the constant $C_{\mathbf{r}}$ does not affect the relative quantum free energies for different values of Λ_n and λ_m.) The quantity in angular brackets is calculated within the reaction coordinate bins during molecular dynamics simulations governed by the mapping potential $V_{map}(\mathbf{r}, \mathbf{R}; \lambda_m)$. We emphasize that, assuming adequate sampling, the use of this perturbation formula is rigorously identical to adiabatic mixed quantum/classical molecular dynamics simulations that include feedback between the quantum and classical subsystems.[21,22]

Thus, both the classical and quantum free energy profiles are obtained from molecular dynamics simulations governed by the mapping potential $V_{map}(\mathbf{r}, \mathbf{R}; \lambda)$. These simulations are performed using GROMOS[18] and a modified FORCE routine. The integration time step is 1 fs, and the constraints are maintained by SHAKE.[23] Two separate

Berendsen thermostats[24] with relaxation times of 0.1ps each maintain the temperature of the solute and the water molecules at 300 K. The equilibration procedure is described in ref 8. After equilibration, we performed 80 ps of data collection for each value of the mapping parameter λ_m (0.0, 0.05, 0.125, 0.25, 0.375, 0.5, 0.625, 0.75, 0.875, 0.95, and 1.0).

C. Dynamical Effects. The transition state theory rate constant k_{TST} defined in eq 3 is based on the assumption that the rate is determined by the forward flux through the dividing surface. Thus, transition state theory assumes that each trajectory passes through the dividing surface only one time.[13] In dynamical systems, the environment may cause trajectories to recross the dividing surface. The "exact" rate constant k_{dyn} including dynamical effects may then be expressed as

$$k_{dyn} = \kappa k_{TST} \quad (10)$$

where κ is the transmission coefficient that accounts for recrossings of the dividing surface.

In standard classical molecular dynamics simulations, κ may be calculated using reactive flux methods for infrequent events.[25−27] In this approach, κ is calculated as the flux-weighted average of a quantity ξ for a canonical ensemble of classical molecular dynamics trajectories started at the dividing surface and integrated backward and forward in time. The quantity ξ corrects for multiple crossings of the dividing surface (i.e., so that all trajectories that originate as reactants and end as products are counted only once, no matter how many times they cross the dividing surface, and all trajectories that go from reactants to reactants, products to products, or products to reactants are not counted at all). In particular, $\xi = 1/\alpha$ for trajectories that have α forward crossings and $\alpha - 1$ backward crossings of the dividing surface, and ξ is zero otherwise.

We incorporate nuclear quantum effects in the calculation of κ by combining the MDQT mixed quantum/classical method[28−30] with this reactive flux method for infrequent events.[8] The fundamental principle of MDQT is that an ensemble of trajectories is propagated, and each trajectory moves classically on a single adiabatic surface except for instantaneous transitions among the adiabatic states. The adiabatic states $\Phi_j(\mathbf{r}; \mathbf{R})$ are calculated at each classical molecular dynamics time step by solving eq 2 with the state-averaged FGH-MCSCF method.[10] The classical nuclei evolve according to Newton's classical equations of motion with the effective potential $\epsilon_k(\mathbf{R})$ (defined in eq 2), where k denotes the occupied adiabatic state. The time-dependent wave function describing the quantum nuclei is expanded in a basis of the adiabatic states

$$\Psi(\mathbf{r}, \mathbf{R}, t) = \sum_{j=0}^{N_{ad}-1} C_j(t) \Phi_j(\mathbf{r}; \mathbf{R}) \quad (11)$$

and the quantum amplitudes $C_j(t)$ are calculated by integrating the time-dependent Schrödinger equation simultaneously with the classical equations of motion. At each time step, Tully's "fewest switches" algorithm[28] is invoked to determine if a quantum transition to another adiabatic state should occur. This algorithm correctly apportions trajectories among the adiabatic states according to the quantum probabilities $|C_j(t)|^2$ with the minimum required number of quantum transitions (neglecting difficulties with classically forbidden transitions).

The use of the standard classical reactive flux approach in conjunction with MDQT is problematic since the probability of nonadiabatic transitions depends on the quantum amplitudes, which depend on the history of the trajectory. Thus, trajectories started at the dividing surface cannot be propagated backward in time with the MDQT method.

(18) Scott, W. R. P.; Hunenberger, P. H.; Tironi, I. G.; Mark, A.; Billeter, S. R.; Fennen, J.; Torda, A. E.; Huber, T.; Kruger, P.; van Gunsteren, W. F. *J. Phys. Chem. A* **1999**, *103*, 3596.

(19) van Gunsteren, W. F.; Beutler, T. C.; Fraternali, F.; King, P. M.; Mark, A. E.; Smith, P. E. In *Computer Simulation of Biomolecular Systems: Theoretical and Experimental Applications*; van Gunsteren, W. F., Weiner, P. K., Wilkinson, A. J., Eds.; Escom: Leiden, The Netherlands, 1993; Vol. 2.

(20) Kirkwood, J. G. *J. Chem. Phys.* **1935**, *3*, 300.

(21) Azzouz, H.; Borgis, D. *J. Chem. Phys.* **1993**, *98*, 7361.

(22) Staib, A.; Borgis, D.; Hynes, J. T. *J. Chem. Phys.* **1995**, *102*, 2487.

(23) Ryckaert, J.-P.; Ciccotti, G.; Berendsen, H. J. C. *J. Comput. Phys.* **1977**, *23*, 327.

(24) Berendsen, H. J. C.; Postma, J. P. M.; van Gunsteren, W. F.; DiNola, A.; Haak, J. R. *J. Chem. Phys.* **1994**, *81*, 3684.

(25) Bennett, C. H. *Algorithms for Chemical Computation*; American Chemical Society: Washington, DC, 1997.

(26) Keck, J. C. *J. Chem. Phys.* **1960**, *32*, 1035.

(27) Anderson, J. B. *J. Chem. Phys.* **1973**, *58*, 4684.

(28) Tully, J. C. *J. Chem. Phys.* **1990**, *93*, 1061.

(29) Hammes-Schiffer, S.; Tully, J. C. *J. Chem. Phys.* **1994**, *101*, 4657.

(30) Hammes-Schiffer, S. *J. Phys. Chem. A* **1998**, *102*, 10443.

(Backward propagation requires knowledge of the quantum amplitudes at the dividing surface, which are unavailable.) To surmount this difficulty, we use the method developed by Hammes-Schiffer and Tully[31] for simulating infrequent events in reactions that evolve on multiple potential energy surfaces.[31] In this approach, trajectories are started at the dividing surface and propagated backward in time with a fictitious surface hopping algorithm that does not depend on the quantum amplitudes. The trajectory is then propagated forward in time, retracing the exact same trajectory, integrating the quantum amplitudes and calculating the probabilities for nonadiabatic transitions for each time step using the true surface hopping algorithm. Each trajectory is assigned a weighting that ensures that the overall results are identitical to those that would have been obtained with the true surface hopping algorithm.

In the implementation of this reactive flux method for MDQT within the framework of the methodology presented in this paper,[8] the weighted average of a quantity x is
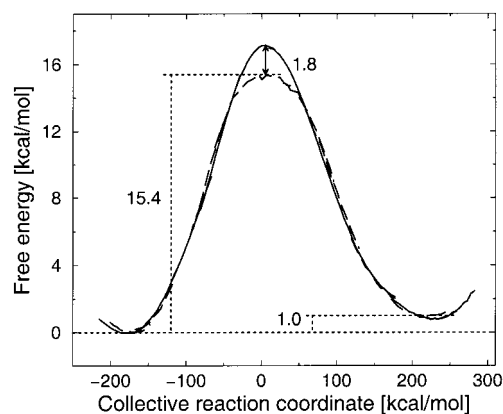
$$\langle x \rangle_w = \frac{\sum_{i=1}^{N_{\text{traj}}} (\dot{\mathbf{R}}_i \cdot \hat{\mathbf{n}}_i) w_i^{\text{can}} w_i^{\text{sh}} x_i}{\sum_{i=1}^{N_{\text{traj}}} (\dot{\mathbf{R}}_i \cdot \hat{\mathbf{n}}_i) w_i^{\text{can}} w_i^{\text{sh}}} \qquad (12)$$

The transmission factor κ is then

$$\kappa = \langle \xi \rangle_w \qquad (13)$$

Here N_{traj} is the number of trajectories required to represent an ensemble, $\dot{\mathbf{R}}_i$ is the initial velocity vector, and $\hat{\mathbf{n}}_i$ is the unit vector normal to the dividing surface. The weightings w_i^{can} ensure a canonical distribution at the dividing surface. These weightings include both a factor accounting for the generation of the ensemble of initial configurations at the dividing surface with the mapping potential and a factor accounting for a Boltzmann distribution over the vibrational adiabatic states at the dividing surface. The weightings w_i^{sh} ensure the correct surface hopping probabilities for each trajectory within the ensemble. These weightings are obtained from the backward propagation with the fictitious surface hopping algorithm and the subsequent forward propagation over the exact same trajectory while integrating the quantum amplitudes and calculating the probabilities of nonadiabatic transitions for the true surface hopping algorithm. (Note that the quantum amplitudes for the forward propagation are initialized such that the quantum amplitude of the occupied state after the backward propagation is unity.) The details of the calculation of κ in this manner are given in ref 8. This weighting procedure is based on the assumption that the MDQT surface hopping algorithm results in an exact Boltzmann distribution among the vibrational states for long times (i.e., after equilibration of the reactant or product). This assumption is not rigorously valid, and the impact of this approximation is currently under investigation.

For the MDQT simulations, the classical equations of motion are integrated using the velocity Verlet algorithm[32] with a time step of 0.5 fs, maintaining the constraints with RATTLE.[33] Note that no thermostat is used for the MDQT simulations, and therefore the nonbonded interactions pairlist is not updated. This aspect of the MDQT simulations is not problematic due to the short duration of each MDQT trajectory. To avoid artifacts due to abrupt changes in momentum, the velocities are not reversed after classically forbidden nonadiabatic transitions. The dividing surface used for the reactive flux method is defined to be $\Lambda^{(q)}(\mathbf{R}) = 0$. The trajectories are propagated in the forward and backward directions until $|\Lambda^{(q)}(\mathbf{R})| > 125.5$ kcal/mol for twenty sequential time steps. This criterion is chosen to indicate that the

(31) Hammes-Schiffer, S.; Tully, J. C. *J. Chem. Phys.* **1995**, *103*, 8528.
(32) Allen, M. P.; Tildesley, D. J. *Computer Simulation of Liquids*; Clarendon Press: Oxford, U.K., 1989.
(33) Andersen, H. C. *J. Comput. Phys.* **1983**, *52*, 24.

Figure 3. Free energy profiles of the hydride transfer reaction as functions of the collective reaction coordinate. The solid line indicates the classical profile, and the dashed line indicates the adiabatic quantum profile (including zero point motion for the transferring hydride). The minimum free energies of the classical and adiabatic quantum profiles are set to zero, and the difference in free energy barriers is indicated. The dotted lines denote experimental values.
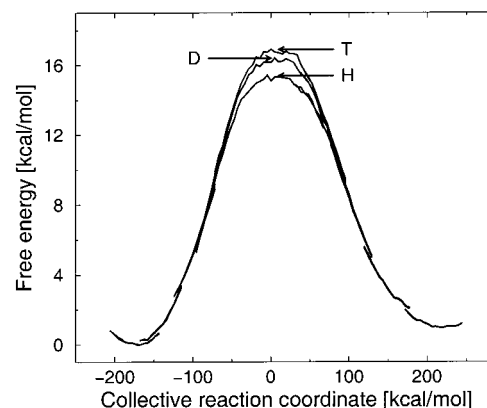
Figure 4. Adiabatic quantum free energy profiles (including zero point motion of the hydride) as functions of the collective reaction coordinate for hydrogen (H), deuterium (D), and tritium (T).

trajectory is out of the strong coupling region and in either the reactant or the product region.

III. Results

A. Equilibrium Properties. The free energy profiles for the transfer of a classical and a quantum mechanical hydride nucleus are compared in Figure 3. The adiabatic quantum free energy profile includes the zero point motion of the transferring hydride. Figure 3 indicates that the nuclear quantum effects substantially decrease the free energy barrier for this reaction. This effect is due to the delocalization of the hydride wave function over both the reactant and product wells in the transition state region. Furthermore, although the shapes of the classical and quantum free energy profiles are very similar in the reactant and product regions, they differ considerably in the transition state region due to the delocalization of the hydride wave function. Note that the coupling between the EVB surfaces V_{12} and the constant energy adjustment Δ_{12} have been chosen such that the quantum free energy profile reproduces the experimental free energies of activation and reaction.

Figure 4 depicts the adiabatic quantum free energy profiles for the transfer of hydrogen, deuterium and tritium. The free energies of activation for these isotopes are 15.4, 16.4, and 16.9 kcal/mol, respectively. Due to the perturbative approach used in these calculations (as given in eq 7), the relative uncertainty
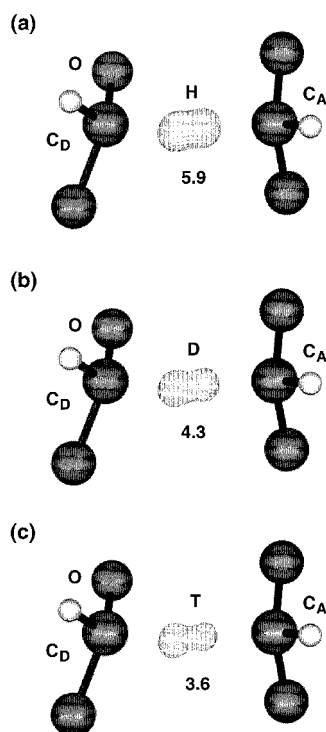
Figure 5. Vibrational wave functions of the transferring hydride for a representative transition state configuration with (a) hydrogen, (b) deuterium, and (c) tritium. On the donor side the alkoxide group and one carbon atom of the ring are shown, while on the acceptor side the acceptor carbon atom and its first neighbors are shown. The vibrational ground states are shown with corresponding energies relative to the lowest grid point given in kcal/mol.

of these values is at most 0.2 kcal/mol.[8] The differences in activation free energies for the three isotopes are due to the varying zero point energies. Figure 5 depicts the hydrogen, deuterium, and tritium vibrational wave functions, together with the corresponding energies relative to the lowest energy grid point, for a representative transition state configuration. This figure illustrates that tritium is much more localized and has a smaller zero point energy than hydrogen. Note that the free energy of activation for tritium is very close to the classical free energy (17.2 kcal/mol).

These differences in the free energy of activation result in kinetic isotope effects of $k_{TST}^H/k_{TST}^D = 5.0 \pm 1.8$ and $k_{TST}^D/k_{TST}^T = 2.4 \pm 0.8$. The corresponding values from experiment are $k_{exp}^H/k_{exp}^D = 3.78 \pm 0.07$ and $k_{exp}^D/k_{exp}^T = 1.89 \pm 0.01$.[1,34] Thus, our calculations slightly overestimate the experimental kinetic isotope effects but are still well within the accuracy of the calculations. These kinetic isotope effects do not yet contain nonequilibrium effects such as dynamical barrier recrossings.

We point out that this hybrid approach is fundamentally different from a standard transition state theory calculation with a classical hydrogen nucleus. In such a standard calculation, the transition state is defined as a first-order saddle point on the potential energy surface, and the reaction coordinate is defined in terms of the minimum energy path (i.e., the path of steepest descent from the transition state toward the reactant and product minima in mass weighted Cartesian coordinates).

(34) Experimentally, k_H/k_T is determined with H in the secondary position, while k_D/k_T is determined with D in the secondary position.[1,2] In our calculations, the secondary position is always hydrogen. Since this secondary hydrogen is treated classically with a constrained bond length, however, the difference between hydrogen and deuterium in the secondary position is negligible.

In this case, the reaction coordinate depends explicitly on the hydrogen coordinate. Zero point energy may be included in these types of standard calculations through harmonic vibrational frequencies determined at the reactant and the transition state, where the imaginary frequency at the transition state (i.e., the mode along the reaction coordinate) is omitted. Additional nuclear quantum effects (e.g., those along the reaction coordinate) may be included in the form of semiclassical tunneling corrections.

In our hybrid approach, the collective reaction coordinate is defined as the difference between the reactant and product valence bond state energies averaged over the ground state hydrogen vibrational wave function. Thus, this collective reaction coordinate does not depend explicitly on the hydrogen coordinate. The transition state is defined to occur when this collective reaction coordinate is zero (i.e., when the hydrogen potential is virtually symmetric). This type of collective reaction coordinate has been used successfully to describe electron[14−17] and proton[9,22] transfer reactions. In our hybrid approach, the zero point motion of the transferring hydrogen nucleus is included along the entire collective reaction coordinate through the representation of this nucleus as a three-dimensional wave function. This quantum mechanical treatment of the hydrogen nucleus is analogous to the quantum mechanical treatment of electrons in electronic structure theory (where the reaction coordinate does not depend explicitly on the electronic coordinates). Hydrogen tunneling effects are incorporated through the combination of these adiabatic quantum free energy profiles and real-time trajectories propagated with the MDQT surface hopping method.
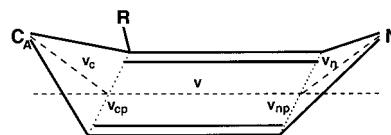
These simulations provide insight into the fundamental nature of the nuclear quantum effects. The splittings between the lowest two hydrogen vibrational states for observed transition states range from 0.64 to 2.3 kcal/mol, with the weighted average splitting being 1.35 kcal/mol. The shapes of the vibrational wave functions indicate that this vibrational excitation corresponds approximately to a stretching mode along the donor−acceptor axis.[8] An analysis of hydrogen tunneling is not straightforward due to the three-dimensional nature of the hydrogen potential and wave function. To aid in our analysis, we calculated the one-dimensional hydrogen vibrational wave functions for the one-dimensional potentials projected along the donor−acceptor axis. (This one-dimensional potential was obtained by choosing the lowest value of the potential energy in the plane perpendicular to the donor−acceptor axis for each grid point along this axis.) We found that the splittings between the lowest energy one-dimensional hydrogen vibrational states are similar to the splittings for the lowest energy three-dimensional vibrational states. (The differences between the one- and three-dimensional splittings are due to coupling among the dimensions.) For the smallest observed splitting (i.e., the highest barrier) at the transition state, the one-dimensional splitting is 0.64 kcal/mol, while the three-dimensional splitting is 0.58 kcal/mol. In this case, the lowest two one-dimensional vibrational states are both below the one-dimensional barrier. For the largest observed splitting (i.e., the lowest barrier), the one-dimensional splitting is 2.28 kcal/mol, while the three-dimensional splitting is 2.33 kcal/mol. In this case, the lowest two one-dimensional vibrational states are both above the one-dimensional barrier. For the average splitting, the lowest one-dimensional vibrational state is ∼0.2 kcal/mol below the one-dimensional barrier. Although this simplified analysis neglects coupling among the dimensions, it provides insight into the nature of the nuclear quantum effects. Specifically, this analysis implies that some

(a)

(b)

(c)

(d)
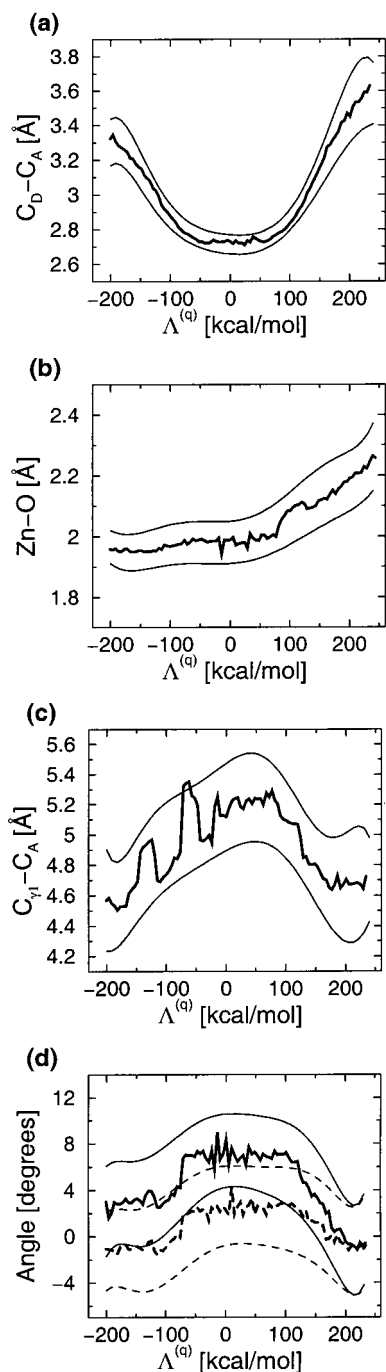
Figure 6. Equilibrium averages of select distances and angles as functions of the collective reaction coordinate $\Lambda^{(q)}$: (a) C_D-C_A distance; (b) $Zn-O$ distance; (c) VAL-203 $C_{\gamma 1}-C_A$ distance; (d) C (solid line) and N (dashed line) NAD$^+$/NADH ring angles (defined in Figure 7). The thin lines represent the average (thick lines) plus the rms deviation, fitted to a polynomial of the sixth order.

Figure 7. Definition of NAD$^+$/NADH ring angles used in Figures 6 and 9 and Table 2. The C angle is defined as the angle between the vectors $\mathbf{v}$ and $\mathbf{v}_c$ projected onto the plane perpendicular to $\mathbf{v}_{cp}$, and the N angle is defined analogously. The C and N angles are defined as positive (pointing toward the substrate) in this figure. R is the amine group.

hydrogen tunneling (i.e., transmittal of probability through a barrier) occurs in the direction along the donor−acceptor axis during the LADH hydride transfer reaction.

Figure 6 depicts the dependence of select distances and angles on the collective reaction coordinate, as determined by averaging over equilibrium molecular dynamics simulations. Note that these equilibrium averages are obtained from simulations driven by the mapping potential (eq 4), so the configurations are weighted by $\exp[-\beta(\epsilon_0(\mathbf{R}) - V_{\mathrm{intmap}}(\mathbf{R}; \lambda_m))]$ as in eq 7. The numerical noise in these data suggests that more than 80 ps of data collection per mapping parameter λ_m would be desirable

to ensure complete convergence for the slowest motions. Nevertheless, considering the RMS deviations indicated in Figure 6, we do not expect the results to change qualitatively with additional data collection. This figure indicates that the reaction coordinate is composed of a variety of motions, including the C_D-C_A distance, the $Zn-O$ distance, the angles in the NAD$^+$/NADH ring (defined in Figure 7), and even the VAL-203 $C_{\gamma 1}-C_A$ distance. Note that the $Zn-O$ distance is determined in part by the bonding structures defined for each VB state, whereas the C_D-C_A and the VAL-203 $C_{\gamma 1}-C_A$ equilibrium distances are not defined in these bonding structures and hence are allowed greater freedom during the reaction.

The analysis of the behavior of these angles and distances along the collective reaction coordinate provides insight into the enzyme mechanism. Figure 6d indicates that the C and N angles in the NAD$^+$/NADH ring increase at the transition state. This result implies that the boat configuration is energetically more favorable than the chair configuration at the transition state. (Despite the limitations of a pairwise additive force field, in this case the force field reproduces the many-body electronic effects favoring the boat configuration.[35]) In the reactant and product, the fluctuations of the two angles average to nearly zero. For the transition state, however, the decrease in the C_D-C_A distance biases the C angle in the NAD$^+$/NADH ring to become positive, which in turn biases the N angle to become positive. The $Zn-O$ distance increases monotonically during the reaction and differs significantly for the reactant and product states. In contrast, the C_D-C_A distance is smallest at the transition state, as expected since the smaller distance decreases the potential energy barrier. The VAL-203 $C_{\gamma 1}-C_A$ distance, however, is largest at the transition state. These trends indicate that the simultaneous motion of the acceptor toward the donor and away from the VAL-203 is a critical component of the reaction coordinate.

These simulations provide an explanation for the experimental observation that replacing VAL-203 by the smaller residue alanine decreases the rate.[3] As shown in Figure 6, throughout the reaction the average $C_{\gamma 1}-C_A$ distance is larger than the contact distance and exhibits a maximum at the transition state. (Here "contact distance" is defined as the minimum of the van der Waals interaction between two atoms.) Our equilibrium simulations indicate that at least one of the following two contact distances is maintained throughout the reaction: (1) The $C_{\gamma 1}$ of VAL-203 is in contact distance with the NAD$^+$/NADH carbon atom bonded directly to C_A, or (2) the $C_{\gamma 2}$ of VAL-203 is in contact distance with a carbon atom in THR-178, which in turn has several atoms in contact distance with C_A. Note that both of these conditions are satisfied in the crystal structure, as shown in Figure 1. The dynamical freedom of maintaining only one of these contact distances may be important for the reaction and will be investigated further. These results suggest that the
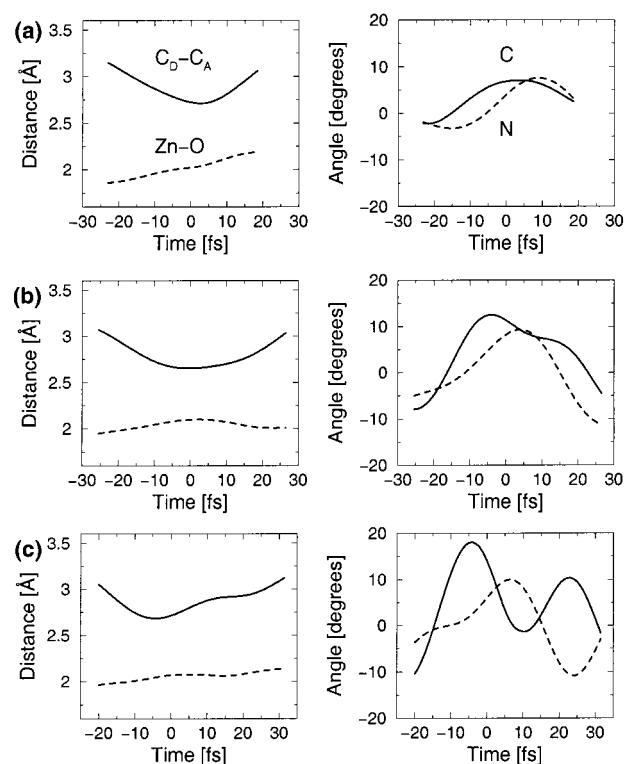
(35) Wu, Y.-D.; Houk, K. N. *J. Org. Chem.* **1993**, *58*, 2043.
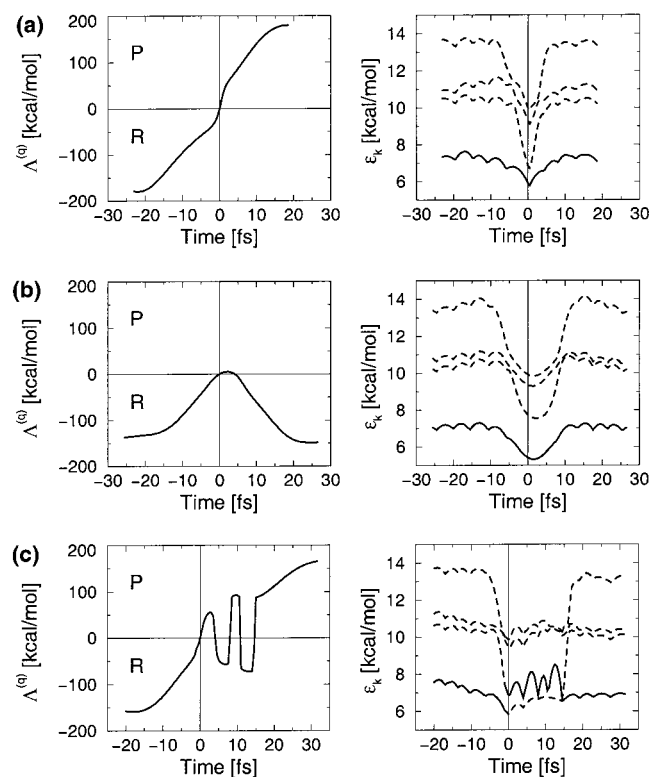
Figure 8. Real-time trajectories of the hydride transfer reaction catalyzed by liver alcohol dehydrogenase. On the left is the reaction coordinate, where R and P indicate the reactant and product sides, respectively. On the right are the four lowest vibrational adiabatic energies relative to the lowest grid point, where the occupied vibrational state is solid. The trajectories shown are the following: (a) productive, no recrossings, no nonadiabatic transitions; (b) nonproductive, one forward and one backward crossing, no nonadiabatic transitions; (c) productive, three forward and two backward crossings, two nonadiabatic transitions.

motion of VAL-203 and THR-178 directs C_A toward C_D through steric interactions. When VAL-203 is replaced with alanine, the C_γ atoms of VAL-203 are no longer available for these steric interactions, leading to a decrease in the rate of hydride transfer.

B. Nonequilibrium Dynamical Properties. As discussed in section II, we propagated an ensemble of real-time trajectories initiated at the transition state to investigate the nonequilibrium dynamical aspects of the LADH reaction. The average length of time for each trajectory was ~50 fs. Figure 8 depicts three representative real-time trajectories of the hydride transfer reaction: a productive trajectory that crosses the dividing surface only once, a nonproductive trajectory that crosses the dividing surface once in the forward and once in the backward direction, and a productive trajectory with three forward crossings and two backward crossings. The first two trajectories do not exhibit any nonadiabatic transitions, while the third trajectory exhibits two nonadiabatic transitions near the dividing surface. The energies ϵ_k of the vibrational states are measured relative to the lowest energy grid point and thus provide an indication of the zero point energy. These energies decrease in the transition state region relative to the reactant and product regions due to greater delocalization of the hydride wave function. In addition, the excitation energies are considerably smaller in the transition state region than in the reactant and product regions, leading to a higher probability of nonadiabatic transitions in the transition state region. Figure 8 illustrates that the first trajectory crosses this transition state region quickly, while the other two trajectories spend much more time there. In the third trajectory,

Figure 9. Real-time trajectories of the hydride transfer reaction catalyzed by liver alcohol dehydrogenase. On the left are the $C_D–C_A$ distance (solid) and the Zn–O distance (dashed). On the right are the C (solid) and N (dashed) angles in the $NAD^+/NADH$ ring, as defined in Figure 7. The trajectories are those shown in Figure 8.

the system is trapped in the first excited state in the transition state region, leading to multiple recrossings of the dividing surface.

Since the hydrogen nucleus is represented as a three-dimensional vibrational wave function, the energies of the hydrogen vibrational states in Figure 8 may be compared to local harmonic bending and stretching modes of typical C–H bonds. For these three trajectories, in the region toward the reactant (between times −20 and −10 fs), the average excitation energies for the three excited vibrational states respectively are ~1100, 1300, and 2200 cm^{-1}. The local harmonic frequencies for typical C–H bond bending and stretching modes are 1400–1500 and 2800–2900 cm^{-1}, respectively.[36] Our calculated frequencies are somewhat lower than these typical values due to anharmonicities excluded in the construction of the potential, coupling among the modes, and the proximity of other atoms in the system, particularly the acceptor carbon atom. Nevertheless, the calculated frequencies agree qualitatively with the typical values obtained from a local harmonic treatment.

Figure 9 depicts the time evolution of select distances and angles during the three trajectories shown in Figure 8. This figure is consistent with Figure 6, which indicates that the $C_D–C_A$ distance, Zn–O distance, and $NAD^+/NADH$ angles contribute to the reaction coordinate. For all three trajectories, the $C_D–C_A$ distance is smallest in the transition state region. For the productive trajectory with no barrier recrossings, the Zn–O distance increases monotonically in time (i.e., as the reaction progresses from reactants to products). In contrast, the Zn–O distance exhibits a maximum in the transition state region for the nonproductive trajectory and exhibits small fluctuations

(36) Pretsch, E.; Seibl, J.; Clerc, T.; Simon, W. *Tables of Spectral Data for Structure Determination of Organic Compounds,* 2nd ed.; Springer-Verlag: Berlin, 1983.
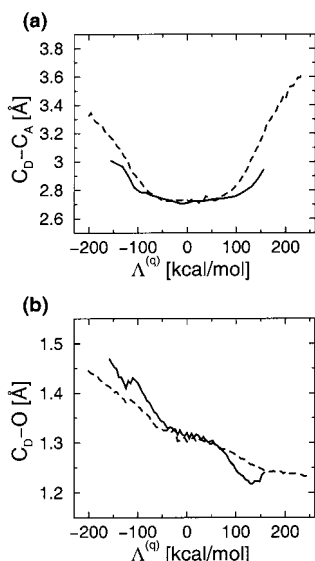
Figure 10. Comparison of equilibrium (dashed) and nonequilibrium (solid) values of distances as functions of the collective reaction coordinate $\Lambda^{(q)}$: (a) C_D-C_A distance; (b) C_D-O distance.

as it increases for the productive trajectory with barrier recrossings. The NAD$^+$/NADH ring angles exhibit the greatest fluctuations for the productive trajectory with barrier recrossings. Note that the two NAD$^+$/NADH angles fluctuate with different frequencies.

Although the time evolution of geometrical properties for individual trajectories provides mechanistic insight into the reaction, averages over an ensemble of trajectories are required to determine the statistical significance of the conclusions. Figure 10 depicts the nonequilibrium values of two select distances as functions of the collective reaction coordinate. These data were obtained from 65 real-time MDQT trajectories propagated backward and forward from the transition state. Note that instead of averaging over all trajectories for each time step, the averages have been calculated within the same bins represented by the collective reaction coordinate $\Lambda^{(q)}$ as used for the free energy profiles. In addition to avoiding difficulties with recrossing trajectories, this procedure allows a comparison between these nonequilibrium values and the equilibrium values to provide an estimate of the time scales of specific motions. Figure 10 indicates that both distances are still far from their equilibrium values at the ends of the short ($\sim$50 fs) real-time trajectories. The C_D-C_A distance has not yet reached its equilibrium distance due to the collective character of this motion. In contrast, the

C_D-O distance has even exceeded its equilibrium distance due to the localized character of this motion.

The transmission coefficients for hydrogen and deuterium were calculated from an ensemble of dynamical trajectories. The calculated values for hydrogen and deuterium were 0.947 and 0.983, respectively, with rms errors of 0.011 and 0.017, respectively. Thus, the difference between the transmission coefficients for hydrogen and deuterium is most likely statistically meaningful. The values of nearly unity for the transmission coefficients suggest that nonequilibrium dynamical effects such as recrossings of the dividing surface are not dominant for this reaction. An inverse kinetic isotope effect of 0.96 is predicted for the transmission coefficients, adjusting the transition state theory value of $k_{TST}^D/k_{TST}^H = 5.0 \pm 1.8$ (given in section IIIA) to 4.8 ± 1.8, which is still in agreement with the experimental value of 3.78 ± 0.07.[2]

We have performed a detailed analysis of the ensemble of trajectories to determine the physical basis for the calculated transmission coefficients. The results of this analysis are summarized in Table 1, which categorizes the trajectories into subsets. The set of hydrogen trajectories in the vibrational ground state at time $t = 0$ is dominated by productive trajectories with no recrossings. This is evident from the large transmission coefficient (0.95) resulting from this set of trajectories, as well as from the large fraction (79%) and significant weight (2.9 compared to 0.54) of trajectories with only a single forward crossing of the dividing surface. Moreover, the recrossings in this subset of trajectories are caused by insufficient flux rather than nonadiabatic transitions. This is indicated by a comparison of the trajectories with only one crossing and the trajectories with more than one crossing: the flux is significantly larger for the former (8.9 versus 2.4 nm/ps), but the number of nonadiabatic transitions is similar for the two types of trajectories (0.13 and 0.12).

The set of hydrogen trajectories in the first excited vibrational state at time $t = 0$ has much lower average weight than the set in the ground state (0.023 compared to 2.4). This difference is mainly due to the Boltzmann factor w^{can} ensuring a canonical distribution at the dividing surface. This set of trajectories is dominated by nonproductive trajectories, as indicated by the fraction of nonproductive trajectories (63%) and the similar weights for all types of trajectories within this set. In this case, the recrossings are caused by trapping in the first excited vibrational state, as indicated by the longer time spent in the coupling region for the trajectories with more than one crossing (15.2 and 18.1 fs) compared to those with only one forward

Table 1. Statistics of MDQT Trajectories of Hydrogen and Deuterium Isotopes[a,b]

	hydrogen								deuterium	
vibrational state at time $t = 0$	0			1				2	0	1
no. of crossings of dividing surface	all	=1	≥2	all	=1	≥2	≥2	all	all	all
trajectory productivity	all	all	all	all	all	non	prod	all	all	all
no. of trajectories in category	257	203	54	130	22	82	26	65	85	58
transmission coeff $\langle\xi\rangle_w = \kappa$	0.95	1	0.00	0.26	1	0	0.40	0.98	0.99	0.39
$\langle$no. of forward crossings$\rangle_w$	1.00	1	1.00	1.70	1	1.52	3.31	1.01	1.00	1.88
$\langle$no. of backward crossings$\rangle_w$	0.04	0	1.07	1.66	0	2.02	2.31	0.13	0.04	1.51
$\langle$tot. time of trajectory$\rangle_w$	45	45	55	53	46	55	58	47	49	54
$\langle$time in coupling region$\rangle_w$[c]	8.3	8.0	17.6	14.6	9.9	15.2	18.1	10.3	8.5	15
$\langle$tot. time in state 1$\rangle_w$	0.9	0.9	1.1	25	15.6	28	24	10.8	3.7	24
$\langle$time in coupling region, state 1$\rangle_w$[c]	0.0	0.0	0.0	13.3	6.7	13.9	20	1.5	0.3	12.7
$\langle$no. of transitions from/into state 1$\rangle_w$	0.13	0.13	0.12	2.3	2.2	2.4	2.1	2.7	0.74	2.9
flux[d]	7.9	8.9	2.4	2.8	20	2.0	6.3	6.9	7.6	2.7
average weight[e]	2.4	2.9	0.54	0.023	0.023	0.022	0.024	0.008	2.1	0.007

[a] $\langle\cdots\rangle_w$ is defined in eq 12. [b] Units are fs for time and nm/ps for flux. [c] The coupling region is defined as $|\Lambda^{(q)}(\mathbf{R})| \leq 62.75$ kcal/mol. [d] Flux = $(\sum_{i=1}^{N_{traj}} w_i^{can} w_i^{sh} \dot{\mathbf{R}}_i \cdot \hat{\mathbf{n}}_i)/(\sum_{i=1}^{N_{traj}} w_i^{can} w_i^{sh})$. [e] Average weight = $\sum_{i=1}^{N_{traj}} \dot{\mathbf{R}}_i \cdot \hat{\mathbf{n}}_i w_i^{can} w_i^{sh}/N_{traj}$.

crossing (9.9 fs). The flux must be very large (average was 20. nm/ps) to avoid this trapping (i.e., to force the trajectory to cross the dividing surface only once). Note that the number of nonadiabatic transitions does not significantly influence recrossings, as indicated by the similar number of nonadiabatic transitions for all types of trajectories within this set. The larger number of nonproductive than productive trajectories with recrossings is due to the difference in the minimum number of crossings required for these two types of trajectories (i.e., at least two for nonproductive and at least three for productive). This trend is apparent from the longer time spent in the coupling region for the productive trajectories (18.1 fs) than for the nonproductive trajectories (15.2 fs) with recrossings. Moreover, the average flux required for a productive trajectory is larger (6.3 nm/ps) than the average flux for a nonproductive trajectory (2.0 nm/ps).

The set of hydrogen trajectories in the second excited state at time $t = 0$ behaves qualitatively similarly to the set in the ground state at $t = 0$. Due to the higher energy, the average weight of the set for the second excited state is somewhat lower than the weight of the set for the first excited state. The second excited state cannot trap the system in the transition state region because, unlike the first excited state, the node of the vibrational wave function is not normal to the donor−acceptor axis.

The deuterium trajectories behave qualitatively similar to the hydrogen trajectories. Due to the smaller splittings between the vibrational states, however, the deuterium trajectories exhibit more nonadiabatic transitions than the hydrogen trajectories for all types of trajectories. As a result, the deuterium trajectories in the ground state at time $t = 0$ spend more time in the first excited state than the corresponding hydrogen trajectories (3.7 versus 0.9 fs), while their total times are comparable. Nevertheless, the time spent in the first excited state while in the coupling region is very small (0.3 fs) even for deuterium trajectories in the ground state at $t = 0$, so the nonadiabatic transitions generally occur too far away from the transition state to cause recrossings due to trapping in the first excited state. As for the hydrogen trajectories, this trapping in the first excited state causes a substantial number of recrossings for trajectories in the first excited state at $t = 0$. The transmission coefficient for these types of trajectories is larger for the deuterium trajectories (0.39 versus 0.26) due to faster relaxation to the ground state, as evident from the larger number of nonadiabatic transitions (2.9 versus 2.3) and the shorter time in the first excited state while in the coupling region (12.7 versus 13.3 fs).

The larger transmission coefficient for the deuterium trajectories in the ground state at $t = 0$ may be understood in terms of the relation between the hydride potential barrier height along the donor−acceptor axis and the energy of the ground state hydrogen vibrational wave function. For simplicity, this relation may be analyzed in terms of one-dimensional hydrogen potentials and wave functions. If the zero point energy is close to the barrier, a small perturbation in the environment will cause one of the two diabatic electronic potential energy surfaces (V_{11} or V_{22}) to become dominant in the region of the hydride potential spanned by the ground vibrational state. As a result, the system will evolve to the reactant or product state quickly, making a barrier recrossing very unlikely. As the zero point energy becomes larger relative to the barrier, both diabatic electronic surfaces will contribute significantly to the electronic ground state in the region of the hydride potential spanned by the ground vibrational state for a wider range of environmental configurations. As a result, the system will spend more time in the transition state region, making barrier recrossings more likely.

Table 2. Normalized Weighted Correlations between Geometrical Properties[a] of the Transition State and the Quantity ξ (Eq 13) for Hydrogen

property	weighted average[b]	weighted rms[c]	normalized weighted correlation[d] (%)
C_D−C_A dist	2.73	0.050	17.8
Zn−O dist	1.98	0.069	0.5
C_D−O dist	1.32	0.020	5.0
VAL-203 $C_{\gamma 1}$−C_A dist	4.97	0.232	5.6
VAL-203 $C_{\gamma 1}$−NH4 dist	5.06	0.277	5.2
VAL-203 $C_{\gamma 1}$−C_D dist	6.97	0.225	0.2
C NAD$^+$/NADH angle	8.62	9.35	−1.7
N NAD$^+$/NADH angle	−2.63	3.16	10.4

[a] Atom names are given in Figure 1. [b] The weighted average for a quantity x is $\langle x \rangle_w$; see eq 12. [c] $\langle (x - \langle x \rangle_w)^2 \rangle_w^{1/2}$ for a quantity x. [d] $\langle (x - \langle x \rangle_w)(y - \langle y \rangle_w) \rangle_w (\langle (x - \langle x \rangle_w)^2 \rangle_w \langle (y - \langle y \rangle_w)^2 \rangle_w)^{-1/2}$ for two quantites x and $y = \xi$.

This trend is verified by our observation that the transmission coefficient increases with barrier height (i.e., as the zero point energy becomes lower relative to the barrier height). On the basis of this analysis, the larger transmission coefficient for deuterium than for hydrogen results from the smaller zero point energy for deuterium (making it smaller relative to the barrier height), which allows fewer barrier recrossings.

We point out that, if the zero point energy were substantially below the barrier, the transmission coefficient would be expected to decrease with barrier height due to increasing probability of nonadiabatic transitions resulting from smaller splittings between vibrational states. Similarly, in this case the transmission coefficient would be expected to be larger for hydrogen than for deuterium. This trend was not observed for this system since the configurations corresponding to such high barrier heights were energetically inaccessible in this ensemble.

Table 2 presents the normalized weighted correlations between the quantity ξ used to determine the transmission coefficient κ (as defined in eq 13) and select geometrical properties at the transition state. To determine the statistical significance of these correlations, we calculated the normalized weighted correlations between ξ and fifty random distances in the system and found the rms of these correlations to be 6.0%.[37] Only the C_D−C_A distance (with a correlation of 17.8%) and the N NAD$^+$/NADH ring angle (with a correlation of 10.4%) are significantly correlated to ξ. Assuming a normal distribution, the probability of obtaining a correlation of ≥17.8% is 0.3%, and the probability of obtaining a correlation of ≥10.4% is 8.3%. The correlation between the C_D−C_A distance and ξ is consistent with the observation that the transmission coefficient increases with the hydride potential barrier height for this system. (The physical basis for this observation is discussed above.) A smaller C_D−C_A distance leads to a smaller barrier and hence decreases the transmission coefficient. On the other hand, a smaller C_D−C_A distance will also contribute to a lower activation free energy, which enters the exponent of k_{TST} in the rate expression (eq 10) and therefore generally dominates the overall rate.

We emphasize that these results do not imply that the geometrical properties uncorrelated with ξ do not influence the enzyme activity. Although such geometrical properties do not influence the nonequilibrium dynamical (i.e., frictional) portion of the reaction rate, they may greatly influence the activation free energy and therefore the transition state theory rate. For

---

(37) Determined using 20 random bond lengths and the distances between 10 random atoms and the donor C_D, acceptor C_A, and secondary hydride NH$_4$ atoms.

example, the distances between the VAL-203 and the reactive center, although not significantly correlated to the barrier recrossings, still significantly impact the activation free energy, as indicated in Figure 6.

IV. Conclusions

This paper presented real-time dynamical simulations of the hydride transfer reaction catalyzed by liver alcohol dehydrogenase. These calculations were performed with a new hybrid approach for the inclusion of nuclear quantum effects such as zero point energy and hydrogen tunneling into real-time dynamical simulations of enzyme reactions.[8] The adiabatic electronic quantum effects of broken and formed bonds are modeled by an empirical valence bond (EVB) potential. This potential requires only two adjustable parameters which have been fit to the experimental free energies of activation and reaction. The adiabatic and nonadiabatic nuclear quantum effects of the transferring hydrogen are included with a mixed quantum/classical approach that represents the transferring hydrogen nucleus by a three-dimensional wave function. The dynamical motion of the complete solvated enzyme is included in these calculations.

The kinetic isotope effects (KIE) for the transfer of hydrogen, deuterium and tritium were calculated from these simulations. The equilibrium transition state theory KIE values were determined from the adiabatic quantum free energy profiles, which include the free energy of the zero point motion for the transferring nucleus. These KIEs were predicted to be $k_{TST}^H/k_{TST}^D = 5.0 \pm 1.8$ and $k_{TST}^D/k_{TST}^T = 2.4 \pm 0.8$. These values are in agreement with the experimental values of $k_{exp}^H/k_{exp}^D = 3.78 \pm 0.07$ and $k_{exp}^D/k_{exp}^T = 1.89 \pm 0.01$. The nonequilibrium dynamical effects were determined by calculating the transmission coefficients with a reactive flux scheme based on real-time molecular dynamics with quantum transitions (MDQT) trajectories. The transmission coefficients, which indicate the degree of dynamical barrier recrossing, were calculated to be 0.947 for hydrogen and 0.983 for deuterium. The values of nearly unity for these transmission coefficients imply that nonequilibrium dynamical effects such as barrier recrossings are not dominant for this reaction. A statistical analysis of the ensemble of MDQT trajectories provided insight into the physical basis for the calculated transmission coefficients. The inclusion of nonequilibrium dynamical effects adjusted the deuterium KIE slightly downward to $k_{dyn}^H/k_{dyn}^D = 4.8 \pm 1.8$.

A statistical analysis of both equilibrium and nonequilibrium simulations was performed to determine the relation between specific enzyme motions and the enzyme activity. The analysis of the equilibrium simulations provided an indication of which geometrical properties impact the activation free energy barrier. The donor–acceptor distance, the catalytic zinc–substrate oxygen distance, and the NAD^+/NADH out-of-plane ring angles were found to strongly impact the activation free energy barrier. The analysis of the nonequilibrium dynamical trajectories provided an indication of which geometrical properties impact the transmission coefficient (i.e., were correlated to the degree of dynamical recrossing of the barrier). The donor–acceptor distance and one of the NAD^+/NADH angles were found to be correlated to the degree of barrier recrossing.

The effect of the donor–acceptor distance on the rate is particularly complex since it impacts both the activation free energy barrier and the transmission coefficient. As the donor–acceptor distance decreases, the transmission coefficient decreases due to the decreased barrier, which leads to more barrier recrossings. On the other hand, the activation free energy barrier decreases as the donor acceptor distance decreases. The overall rate is determined by a competition between these two effects. Since the free energy barrier generally dominates in the rate expression, the overall rate increases as the donor–acceptor distance decreases.

This analysis also provided insight into the experimental observation that the enzyme activity decreases when VAL-203 is substituted by the smaller residue alanine.[3] We found that the distance between VAL-203 and the reactive center significantly impacts the activation free energy but is not correlated to the degree of barrier recrossing. Thus, this effect on the enzyme activity is due to the alteration of the equilibrium free energy difference between the transition state and the reactant rather than nonequilibrium dynamical factors. Our results indicate that the motion of the acceptor carbon away from VAL-203 and toward the donor carbon is a critical component of the reaction coordinate. These simulations also suggest that the motion of VAL-203 and THR-178 directs the acceptor carbon toward the donor carbon through steric interactions involving the C_γ atoms of VAL-203. When VAL-203 is replaced with alanine, the C_γ atoms of VAL-203 are no longer available for these steric interactions, leading to a decrease in the rate of hydride transfer. A more detailed analysis of the effects of this mutation will be provided by future simulations on the mutant LADH enzyme.

To summarize, this investigation provides further insight into several aspects of the LADH-catalyzed hydride transfer reaction. Nonequilibrium dynamical effects such as barrier recrossings were found to be nearly negligible. Nevertheless, links between the geometrical properties of the enzyme and nonequilibrium dynamical effects were identified. In addition, evidence of hydrogen tunneling in the direction along the donor–acceptor axis was obtained. Several promoting motions were identified and characterized, including the donor–acceptor, catalytic zinc–substrate oxygen, NAD^+/NADH ring, and VAL-203 motions. (Here promoting motions refer to systematic changes in thermally averaged geometrical properties as the reaction evolves from the reactant to the transition state.) These average motions occur on the time scale of the hydride transfer reaction (i.e., tens of milliseconds[39]). Furthermore, the catalytic role of steric interactions involving VAL-203, THR-178, and the coenzyme was elucidated.

The hybrid approach implemented in this paper provides insight into the relation between enzyme dynamics and function. In particular, this approach allows the analysis of the impact of specific motions of the enzyme on the activation free energy barrier and on the degree of barrier recrossing. This type of analysis distinguishes between equilibrium and nonequilibrium dynamical factors and thus elucidates the fundamental physical principles of enzyme mechanisms. Furthermore, as illustrated in this paper, this approach will aid in the identification of mutation sites for influencing the enzyme activity.

(38) Ramaswamy, S.; Eklund, H.; Plapp, B. V. *Biochemistry* **1994**, *33*, 5230.

(39) Shearer, G. L.; Kim, K.; Lee, K. M.; Wang, C. K.; Plapp, B. V. *Biochemistry* **1993**, *32*, 11186.